Mesoscale organization, entrainment, and the properties of a closed-cell stratocumulus cloud

J. Kazil[1,2] ⓘ, T. Yamaguchi[1,2] ⓘ, and G. Feingold[2] ⓘ

[1]Cooperative Institute for Research in Environmental Sciences, University of Colorado, Boulder, Colorado, USA, [2]NOAA Earth System Research Laboratory, Chemical Sciences Division, Boulder, Colorado, USA

Abstract Closed-cell mesoscale organization and its relationship to entrainment and the properties of a low, nonprecipitating stratocumulus cloud is investigated. Large eddy simulations were run over 10 periodic diurnal cycles during which mesoscale organization could fully develop and approach a quasi-steady state on five domains sized from 2.4 km × 2.4 km to 38.4 km × 38.4 km. The four smaller domains hosted a single cell with an aspect ratio that increased with domain size. On the largest domain, mesoscale organization consisted of a cell population that evolved over the course of the diurnal cycle. It is found that with increasing cell aspect ratio, entrainment weakens and the boundary layer becomes shallower, cooler, moister, and more decoupled. This causes an increase in cloud water path and cloud radiative effect up to a cell aspect ratio of 16. With further increase in cell aspect ratio, circulation on the cell scale becomes less effective in supplying moisture to the cloud and in producing turbulent kinetic energy (TKE). This mechanism can explain scale saturation in closed-cell mesoscale organization. The simulations support a maximum stable aspect ratio of closed-cell mesoscale organization between 32 and 64, consistent with the observational limit of ≈ 40. The simulations show furthermore that entrainment does not, in general, scale with buoyant production of TKE. Instead, entrainment correlates with the vertical component of TKE. This implies vertical motion as a driver of entrainment, and a convective velocity scale based on the vertical component of TKE rather than on buoyant production of TKE.

1. Introduction

Stratocumulus clouds exhibit regular patterns on the mesoscale, including bands and several types of cells [*Graham*, 1933; *Krueger and Fritz*, 1961; *Agee*, 1984]. These patterns reflect different states of boundary layer circulation [*Atkinson and Zhang*, 1996]. The closed-cell stratocumulus cloud state is characterized by a boundary layer circulation in which updrafts create high optical depths in broad cell centers, and downdrafts result in reduced optical depths around the cell periphery [*Moyer and Young*, 1994; *Atkinson and Zhang*, 1996]. *Shao and Randall* [1996] found that this circulation pattern arises by the action of cloud top cooling. Closed-cell stratocumulus clouds occur predominantly over the subtropical eastern oceans and in midlatitude storm track regions [*Agee et al.*, 1973; *Agee*, 1987; *Wood and Hartmann*, 2006; *Muhlbauer et al.*, 2014]. Along with other marine boundary layer cloud types they exert a strong leverage over reflected solar radiation [*Hartmann and Short*, 1980; *Hartmann et al.*, 1992]. Their shortwave reflectance is higher compared to other marine boundary layer cloud types primarily due to a higher cloud fraction [*Muhlbauer et al.*, 2014]. Closed cell sizes typically range from 10 to 60 km and cell aspect ratios (horizontal size vs. boundary layer depth) from 30:1 to 40:1, with larger cells occurring in deeper boundary layers [*Wood and Hartmann*, 2006].

Horizontal scales of stratocumulus closed-cell circulation are larger than the typical domain sizes of high-resolution simulations (on the order of a few km) that are used in the study of boundary layer clouds. This has prompted investigations of a potential contribution of closed-cell mesoscale organization to boundary layer and stratocumulus properties. *de Roode et al.* [2004] posed the question "Large-eddy simulation: how large is large enough?" They found that with increasing domain size, mesoscale fluctuations in a closed-cell stratocumulus cloud increasingly contributed to vertical transport and to buoyant production of turbulence kinetic energy (TKE), and controlled the field of any quantity, except for the vertical velocity. Horizontal domain size had only a limited influence on the temporal evolution of mean quantities. de Roode et al. concluded that for the study of the spatial evolution of any quantity in the stratocumulus-topped boundary

layer except vertical velocity, domain size should be chosen to be large enough to allow for the autonomous development of mesoscale organization. Other studies also found no support for a contribution of mesoscale organization to mean boundary layer and cloud properties. *Duynkerke et al.* [2004] conducted large eddy simulations of a stratocumulus cloud on a 2.5 and 25.6 km domain. Although mesoscale organization formed on the larger domain, the cloud water path did not show a clear difference between the simulations, and Duynkerke et al. concluded that the mean state of the boundary layer in the simulations was consistent between the two. *Pedersen et al.* [2016] studied the stratocumulus-topped boundary layer with large eddy simulations on domain sizes between 3.5 and 21 km, and found no significant impact of domain size on cloud properties such as cloud fraction and cloud water path.

Domain size dependences have been found in simulations of other cloud types. *Wyant et al.* [1997] studied the transition from stratocumulus to cumulus clouds with a two-dimensional eddy-resolving model. They found slower entrainment and a reduced cloud fraction on a larger (12 km) domain compared to a smaller (3 km) domain. They interpreted the slower entrainment to be a consequence of the reduced cloud fraction, which in turn was associated with the dissipation of detrained stratus on the larger domain. *Stevens et al.* [2002] investigated trade cumulus clouds underlying stratocumulus clouds. Comparing simulations on different domain sizes, they found slower entrainment on the larger domain but no clear separation in cloud water path between the domain sizes. However, they found strong mesoscale variability in cloud water path and concluded that large domain sizes are required to obtain meaningful cloud statistics for this cloud type. Very large domain sizes (tens of kilometers) have been found essential for the study of the open-cell stratocumulus state [*Wang and Feingold*, 2009a, 2009b; *Feingold et al.*, 2010; *Kazil et al.*, 2011]. The associated boundary layer circulation is nonstationary and maintained by the periodic interaction between precipitation and surface convergence/divergence [*Feingold et al.*, 2010]. Domain sizes that are too small fail to produce this interaction, and the open-cell pattern, because the domain quickly becomes filled with a single cell that interacts with itself via periodic lateral boundary conditions.

In this work, closed-cell mesoscale organization in a low, nonprecipitating, quasi-steady state stratocumulus cloud is studied. The relationship between cell aspect ratio and entrainment, decoupling, and cloud properties is investigated and the underlying mechanisms are identified. The evolution of mesoscale organization over the course of the diurnal cycle is characterized and a mechanism for scale saturation is presented. The implications of domain size choice in simulating closed-cell stratocumulus clouds are discussed. Section 2 describes the model and the simulations; results are presented in section 3 and discussed in section 4. Conclusions are given in section 5.

2. Model and Simulations

The System for Atmospheric Modeling [*Khairoutdinov and Randall*, 2003] was configured to simulate a stratocumulus cloud in present-day climate (CGILS S12 CTL) [*Blossey et al.*, 2013]. We used the CGILS S12 CTL initial conditions, boundary conditions, and large-scale forcing with specific modifications. The simulations were initialized with the temperature and moisture profiles for the CGILS S12 CTL case. We used a nudging procedure for their maintenance over the course of the simulations above 1200 m, with a 1 h nudging time scale [*Blossey et al.*, 2013, Appendix A1]. Sea surface temperature was 290.96 K. Large-scale subsidence was calculated from the CGILS S12 CTL vertical pressure velocity. We applied the CGILS S12 CTL present-day horizontal temperature advective tendency at all altitudes and the horizontal moisture advective tendency only in the boundary layer to prevent excessive drying above the inversion [*Blossey et al.*, 2013, Appendix A4]. Advective tendencies were constant across altitudes in the boundary layer with values of -1.1 K d^{-1} and -0.64 g kg^{-1} d^{-1}. We prescribed a constant geostrophic wind with a west-east component of 2.5 m s^{-1} and a south-north component of -10 m s^{-1} but let the dynamical core of the model operate only on the residual wind field. The surface fluxes of momentum, heat, and moisture were calculated from the total (residual + geostrophic) wind speed based on similarity theory and contributed to the residual circulation by production of TKE due to buoyancy and shear. This is akin to moving the domain with the geostrophic wind, although its geographic location remains fixed [*Kazil et al.*, 2014, 2016]. This setup differs from the CGILS specification in which the mean wind speed is nudged toward prescribed profiles and the surface heat and moisture flux are calculated with a dedicated formula [*Blossey et al.*, 2013, Appendix A3]. Our

simulations have a mean 10 m wind speed of 8.4 m s^{-1}, similar to the surface wind speed of 8.3 m s^{-1} obtained by *Blossey et al.* [2013].

Cloud microphysics was represented with a two-moment bin-emulating method that calculates mass and number mixing ratios of cloud and raindrops [*Feingold et al.*, 1998; *Wang and Feingold*, 2009a, 2009b]. Activation was calculated from supersaturation and the local aerosol concentration. A lognormal aerosol size distribution was assumed with a geometric mean diameter of 200 nm and a geometric standard deviation of 1.5. Interstitial aerosol number mixing ratio was nudged with a time constant of 5 min to maintain the total (cloud-borne + interstitial) aerosol number mixing ratio at 100 m g^{-1}. A geometric standard deviation of 1.2 was assumed for both the lognormal cloud and rain drop size distributions. Precipitation did not form in the simulations and horizontal mean rain water mixing ratio remained below 4×10^{-4} g kg^{-1}. Radiation was treated with the rapid radiative transfer model (RRTM) [*Mlawer et al.*, 1997] with profiles according to the CGILS S12 CTL specification added above the domain top to represent the full atmospheric column. The CO_2 mixing ratio was 355 ppm, the surface albedo 0.07, and the surface emissivity 0.95. Advection of scalars was treated with ULTIMATE-MACHO [*Yamaguchi et al.*, 2011].

The simulations were conducted on domains $D_{i=1,\ldots,5}$ ranging in size from 2.4 km $\times$ 2.4 km to 38.4 km $\times$ 38.4 km, with a horizontal side length $L_i = 2.4 \cdot 2^{(i-1)}$ km and a vertical extent from 0 to 1600 m. The model grid spacing was $\Delta x = \Delta y = 50$ m (horizontal), $\Delta z = 10$ m (vertical), and $\Delta t = 1$ s (time) (grid spacing G_1). Sensitivity to grid spacing was tested with $\Delta x = \Delta y = 25$ m, $\Delta z = 5$ m, $\Delta t = 0.5$ s (grid spacing G_2), which corresponds to the CGILS S12 CTL specification. Periodic lateral boundary conditions were used. The domains were located at 35°N, 125°W. The simulations iterated 10 times a diurnal cycle beginning at sunset on 15 July, following *Blossey et al.* [2013]. Longwave and shortwave radiation was updated every 10 s. Output was sampled every 5 min. The role of grid spacing, of the radiation time step length, and of the convergence toward a quasi-steady state are documented in the supporting information.

3. Results

3.1. Mesoscale Organization

Figure 1 shows the evolution of closed-cell mesoscale organization over the course of the diurnal cycle on the largest domain (D_5). The size and shape of cells evolve with time of day. At sunset (Figure 1a), the cloud features small, elongated cells between a few and about 10 km wide. The cells align approximately with the large-scale wind direction (346°). Over the course of the night, mesoscale organization evolves toward larger, more circular, and more optically thick cells (Figure 1b). Cell growth continues during daytime and cell diameters approach 20 km shortly before noon, but insolation reduces cloud optical depth along cell peripheries (Figure 1c). A daytime cell size around 20 km at a boundary layer depth of $\simeq 600$ m (cf. supporting information Figure S8a) is consistent with daytime satellite observations: *Wood and Hartmann* [2006] found a closed cell size of 18 ± 3.9 km at a boundary layer depth of 575 m and of 26 ± 3.4 km at a boundary layer depth of 650 m. Large cells persist into the afternoon but they gradually fade and yield to smaller cells. An individual large cell is present at 21 h, surrounded by smaller cells (Figure 1d). By sunset all large cells have vanished and the system has assumed a small cell configuration (Figure 1a). Mesoscale organization on all domains (D_1–D_5) is documented in the supporting information.

The spatial structure of boundary layer circulation will be investigated with spectral analysis. The spectrum of a quantity Q is expressed as dQ/dk with the wave number $k = \sqrt{k_x^2 + k_y^2}$, where k_x and k_y are horizontal Fourier decomposition wave numbers. Scale is based on the wavelength $\lambda = 1/k$. We will use scale ranges defined by *Orlanski* [1975]. The microscale comprises wavelengths below and the mesoscale wavelengths above 2 km. Within the mesoscale, we will additionally distinguish the cell scale $\hat{\lambda}$ (wavelength at which the spectrum peaks) and intermediate scales which are below the cell scale but above the microscale. The median wavelength λ_{50} of a spectrum is defined as

$$\int_0^{1/\lambda_{50}} dk \frac{dQ}{dk} = \int_{1/\lambda_{50}}^{\infty} dk \frac{dQ}{dk} \tag{1}$$

Figure 2 shows spatial spectra of buoyant TKE production (TKE$_b$) in the boundary layer, and of the vertical resolved-scale flux of total moisture (q_t) at mean cloud base. The spectra identify scales on which TKE
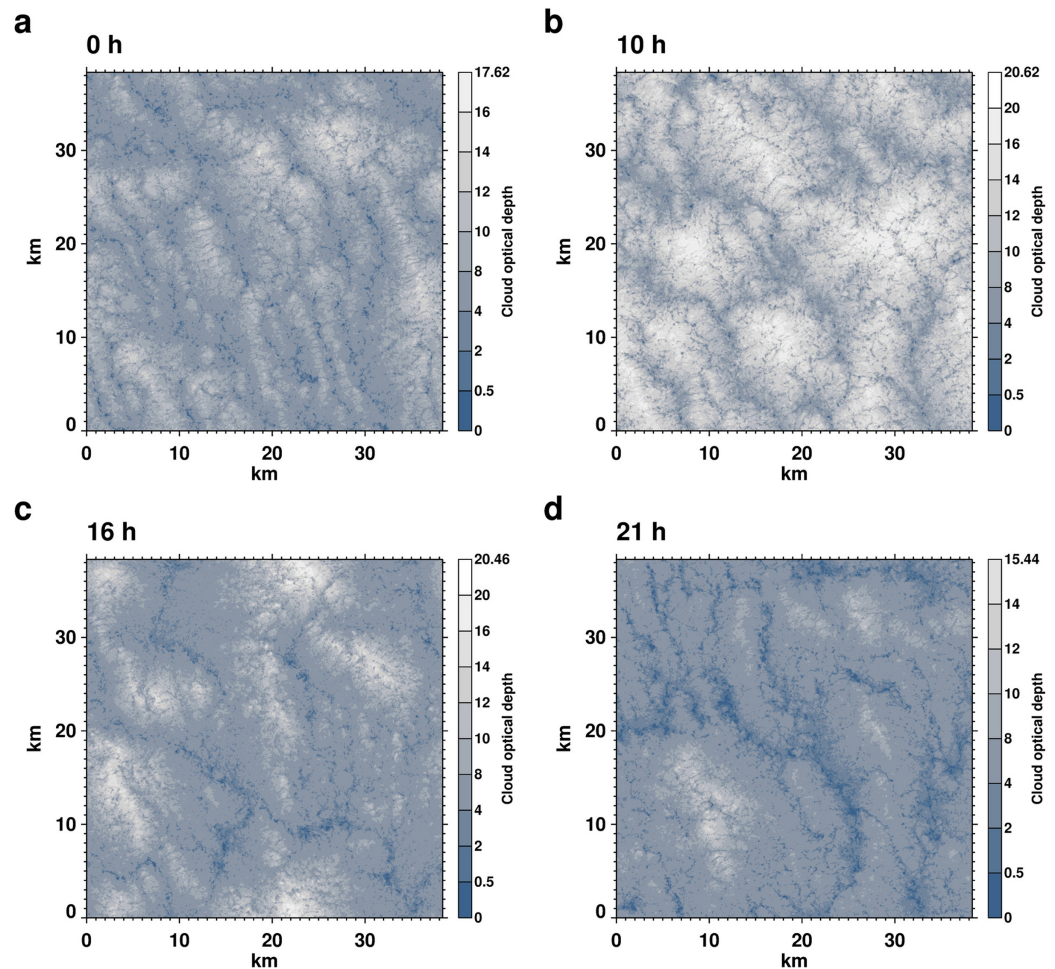
Figure 1. Cloud optical depth on domain D_5 (day 10): (a) sunset, (b) sunrise, (c) 1 h before, and (d) 4 h after noon.

production drives boundary layer dynamics and on which circulation supplies moisture from the subcloud layer to the cloud layer, respectively.

On D_1–D_4, TKE production and vertical moisture transport take place without a discernible scale evolution over the course of the diurnal cycle (Figures 2a–2h). Mesoscale evolution is present on D_5 (Figures 2i and 2j): Cell size increases from 10 km during nighttime to 20 km shortly before noon (17 h). TKE production and moisture flux on the largest scales on D_5 fade toward the evening and are replaced by TKE production and moisture flux on smaller scales, including the 10 km scale from which mesoscale organization forms in the next diurnal cycle. The cell scale on D_5 is separated from smaller scale circulation by the wavelength $L_5/5 = 7680$ m.

With increasing domain size, mesoscale organization becomes increasingly polydisperse owing to the emergence of circulation at intermediate scales (solid triangles in Figure 2). In the cloud field, the polydispersion takes the form of cellular structures embedded into the cell scale on the smaller domains D_1–D_4 (e.g., supporting information Figures S1b, S1f, S1j, S1n, and S1r). On D_5, cellular structures on intermediate scales are also present between larger cells (Figure 1).

Insolation acts as a filter which suppresses circulation on intermediate scales (Figure 2). This suppression strengthens with domain size. The median wavelength (Figure 2) indicates, by its deviation relative to nighttime, the scale toward which TKE production and moisture transport are shifted during daytime due to the suppression of the intermediate scales. On the domains D_1–D_3 (Figures 2a–2f), TKE production and moisture transport are shifted toward the microscale, while on D_4–D_5, they are shifted toward the mesoscale. A stronger suppression of turbulence on scales smaller than the cell scale due to a reduced cloud top cooling
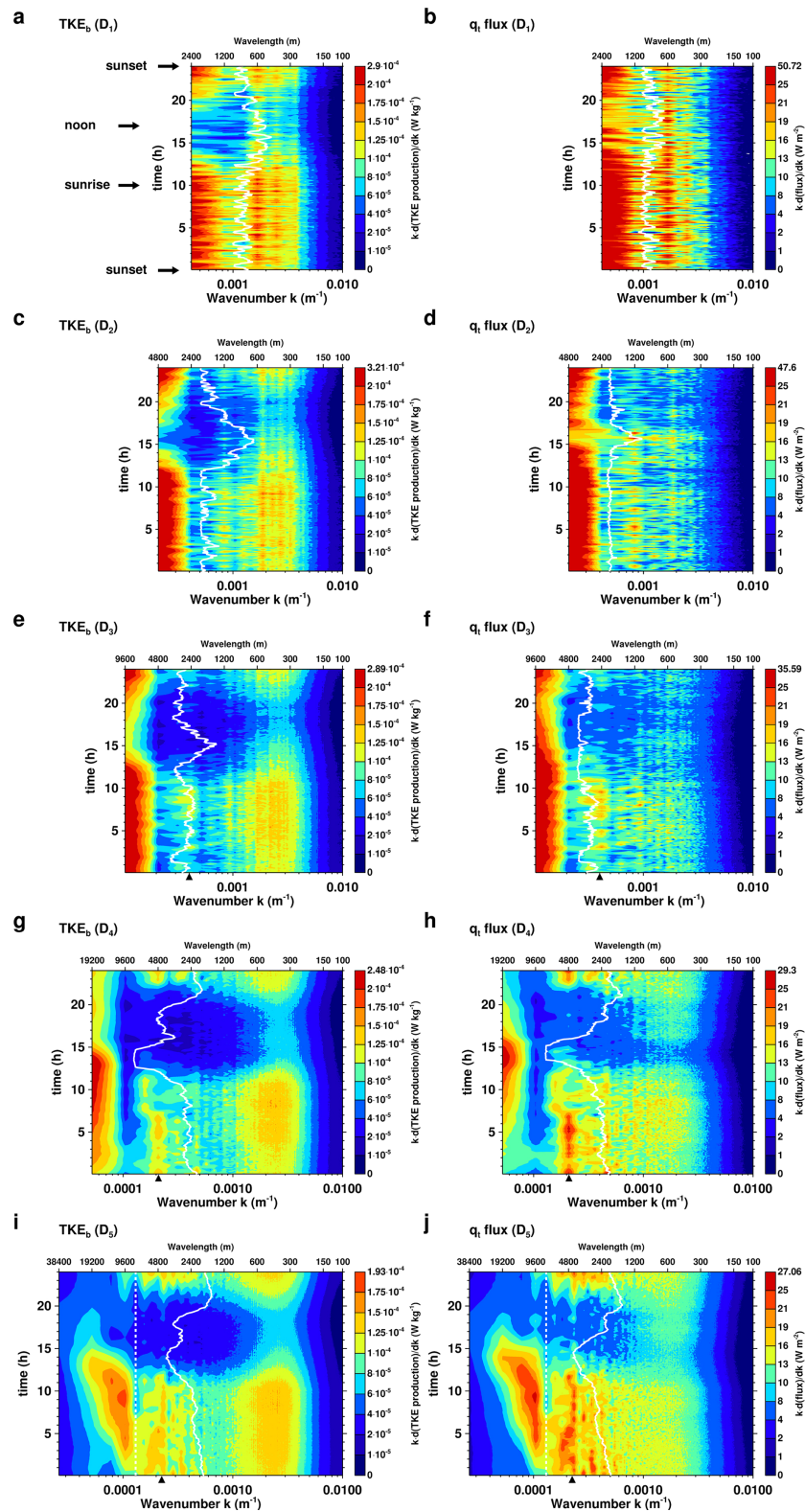
Figure 2. Mean spectra (day 8–10) of buoyant TKE production in the boundary layer and of the vertical resolved-scale flux of total water at mean cloud base. The median wavelength is marked with a solid line. On D_5, the cell scale is separated from smaller scale circulation by the wavelength $L_5/5 = 7680$ m (dashed line). Circulation on intermediate scales that emerges with increasing domain size between the microscale and the cell scale is marked with solid triangles.
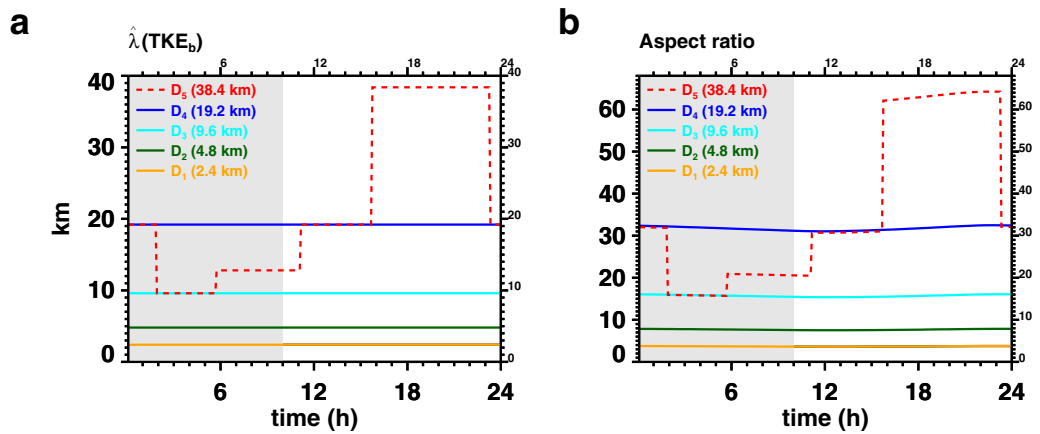
Figure 3. (a) Mean diurnal cycle (day 8–10) of the cell scale ($\hat{\lambda}$) of buoyant TKE production in the boundary layer, and (b) aspect ratio of cell scale circulation, calculated as the ratio of cell scale and inversion height. Gray shading indicates nighttime.

during daytime is consistent with the findings of *Pino et al.* [2006], who determined that in a dry convective boundary layer, small-scale fluctuations dissipate faster than large-scale fluctuations in response to a reduced surface forcing.

Figure 3a shows the diurnal cycle of the cell scale $\hat{\lambda}$ of buoyant TKE production. $\hat{\lambda}$ is constant and matches the domain size on D_1–D_4 (Figure 3); hence, a single cell dominates these domains throughout the diurnal cycle. Figure 3b shows the aspect ratio of cell scale circulation, calculated as $\hat{\lambda}/\overline{z_i}$, with the domain-averaged inversion height $\overline{z_i}$ (overline denotes the instantaneous domain mean throughout this work). The diurnally averaged aspect ratios (day 8–10) on the individual domains are 3.7 (D_1), 7.7 (D_2), 15.7 (D_3), and 31.7 (D_4). On D_5, $\hat{\lambda}$ evolves, reflecting the diurnal cycle in mesoscale organization (Figures 1 and 2i, and 2j). Visual inspection of the mesoscale structure (Figure 1) together with the diurnal cycle $\hat{\lambda}$ (Figure 3) indicates that cell aspect ratio varies from ≈ 4 to 16 at dusk, to 64 in the late afternoon on D_5. The diurnally averaged aspect ratio (day 8–10) on D_5 is 36.6. The rounded aspect ratio values of 4 (D_1), 8 (D_2), 16 (D_3), 32 (D_4), and 37 (D_5) will be used throughout the remainder of this work.

Figure 4 shows decoupling and characteristic scales of TKE production and moisture transport. Decoupling is quantified with the relative decoupling index $(\overline{z_{CB}} - \overline{z_{LCL}})/\overline{z_{LCL}}$, based on the absolute decoupling index $\overline{z_{CB}} - \overline{z_{LCL}}$ introduced by *Jones et al.* [2011]. $\overline{z_{CB}}$ is the mean cloud base height, and $\overline{z_{LCL}}$ the mean lifting condensation level. A higher decoupling index indicates a reduced ability of circulation to transport moisture from the surface to cloud base. Decoupling increases with domain size on D_1–D_4. Circulation on D_1–D_4 is
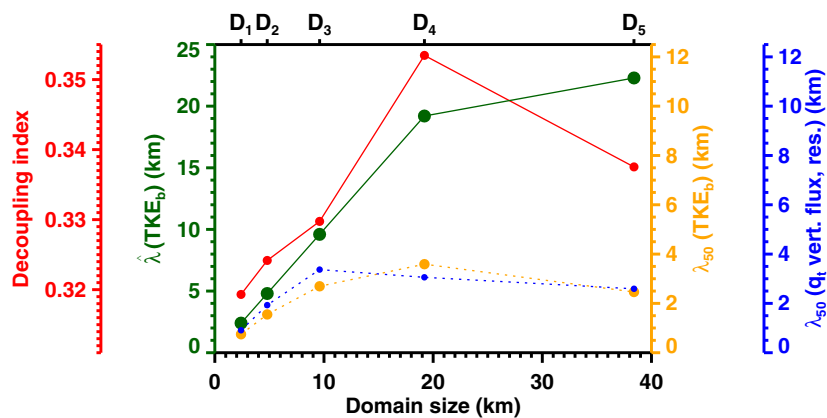
Figure 4. Decoupling index and cell scale ($\hat{\lambda}$) of buoyant TKE production in the boundary layer, and median scale (λ_{50}) of buoyant TKE production in the boundary layer and of the vertical resolved-scale flux of total water at mean cloud base, day 8–10.
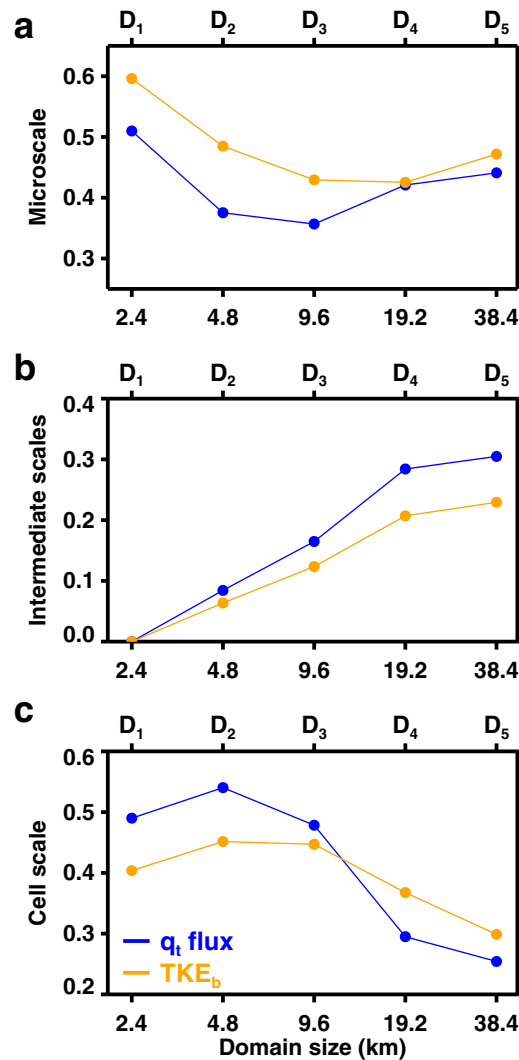
Figure 5. Fractional contribution of the (a) microscale, (b) intermediate scales, and (c) cell scale to buoyant production of TKE in the boundary layer and to the vertical resolved-scale flux of total water at mean cloud base, day 8–10. The contributions were obtained by integrating the spectra in Figure 2. The microscale comprises wavelengths up to 2 km. The contribution of the cell scale was calculated from the value of the spectrum at its maximum, except on domain D_5, where the contribution of the cell scale was calculated by integrating wavelengths $> L_5/5 = 7680$ m (cf. Figures 2i and 2j). Intermediate scales are located between the microscale and the cell scale.

dominated by a single mesoscale cell, and we infer that decoupling increases with cell aspect ratio. Decoupling drops toward D_5 which hosts a cell population with a wide aspect ratio range.
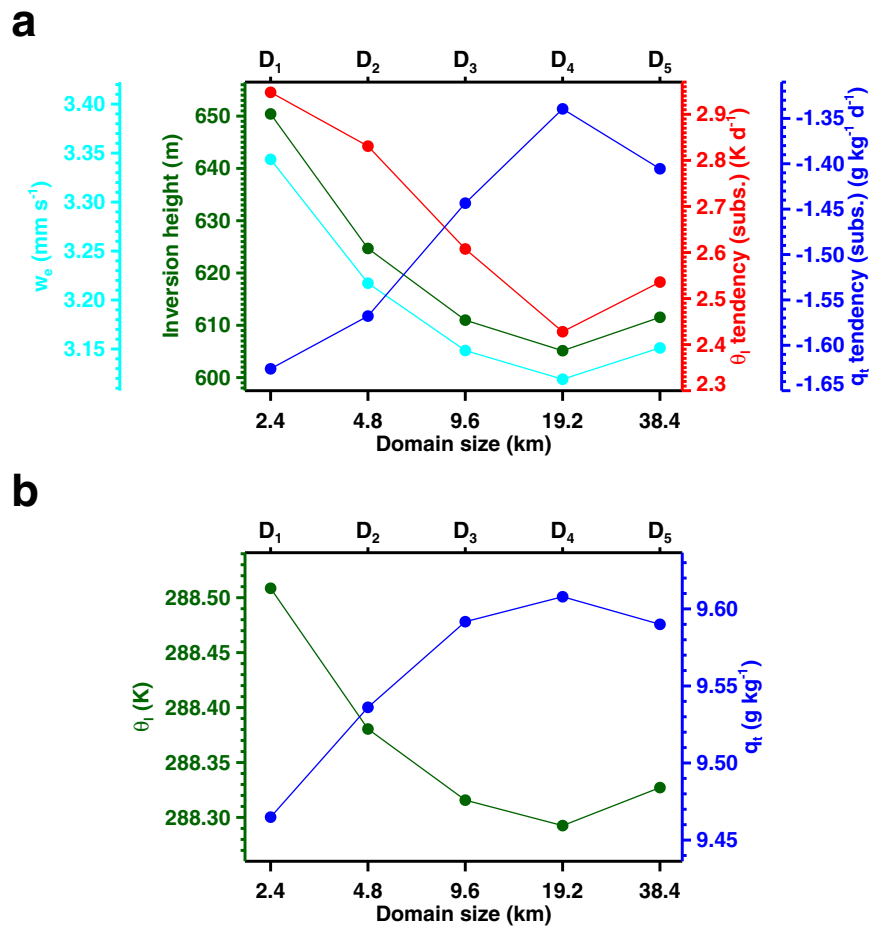
The cell scale $\hat{\lambda}$ becomes increasingly disconnected from the median scale of TKE production and moisture transport (Figure 4). As $\hat{\lambda}$ increases, the median scales of TKE production and moisture transport do so only initially and eventually regress. Hence at larger cell aspect ratios and higher boundary layer decoupling, scales smaller than the cell scale gain importance in driving circulation and supplying moisture to the cloud. Figure 5 gives the fractional contribution of the microscale, intermediate scales, and of the cell scale to buoyant production of TKE in the boundary layer and to moisture supply to the cloud through mean cloud base. The contribution of intermediate scales (solid triangles in Figure 2) to moisture supply to the cloud increases with domain size and cell aspect ratio. On D_1–D_3, intermediate scales contribute $< 20\%$, less than the cell scale ($\simeq 50\%$). On D_4, the contribution of intermediate scales and of the cell scale are similar with a value near 30%. On D_5, the moisture supply to the cloud on the cell scale falls below the contribution of the intermediate scales. The contribution of intermediate scales to TKE production also increases with domain size but remains below the continuously decreasing contribution of the cell scale.

Therefore, with increasing cell aspect ratio, decoupling increases and circulation on the cell scale becomes increasingly ineffective in supplying moisture to the cloud layer and producing TKE. Mesoscale circulation on scales smaller than the cell scale gains importance in supplying moisture to the cloud layer and to a lesser extent in producing TKE.

3.2. Boundary Layer and Cloud Properties

Boundary layer and cloud properties in the diurnally averaged quasi-steady state are presented. The diurnal cycle of boundary layer and cloud properties is documented in the supporting information.

3.2.1. Entrainment, Temperature, and Moisture

Boundary layer circulation drives different rates of entrainment on the different domains. With increasing domain size (D_1–D_4), entrainment decreases, the inversion descends, subsidence warming and drying weaken, and the boundary layer cools and moistens (Figure 6). Entrainment velocity was calculated as $w_e = d\overline{z_i}/dt - w_{sub}(\overline{z_i})$, with the prescribed large-scale subsidence velocity w_{sub}. The reduction in entrainment runs counter to boundary layer energetics and inversion stability: these would, barring other considerations, support an increase in entrainment with domain size. TKE, as well as buoyant production of TKE increase from D_1–D_4, while inversion stability, quantified by the jump in virtual potential temperature across the inversion $\Delta_i \langle \theta_v \rangle$, decreases (Figure 7). Since an individual mesoscale cell occupies D_1–D_4, we deduce that increasing cell aspect ratio hampers entrainment. Boundary layer energetics, cell aspect ratios, and entrainment are discussed in section 4.2.

a

b

Figure 6. (a) Entrainment velocity w_e, inversion height, and boundary layer tendency of total moisture mixing ratio q_t and liquid water potential temperature θ_l due to subsidence, and (b) boundary layer mean liquid water potential temperature θ_l and total moisture q_t, day 8–10.

On D_5, mesoscale organization consists of a cell population with a temporally evolving, polydisperse aspect ratio distribution (Figures 1–3). Under the hypothesis that the dependence of entrainment on cell aspect ratio found on D_1–D_4 holds for individual cells in the mesoscale structure of D_5, the entrainment rate on D_5 is a composite of contributions from the individual cells, codetermined by their aspect ratios. The overall
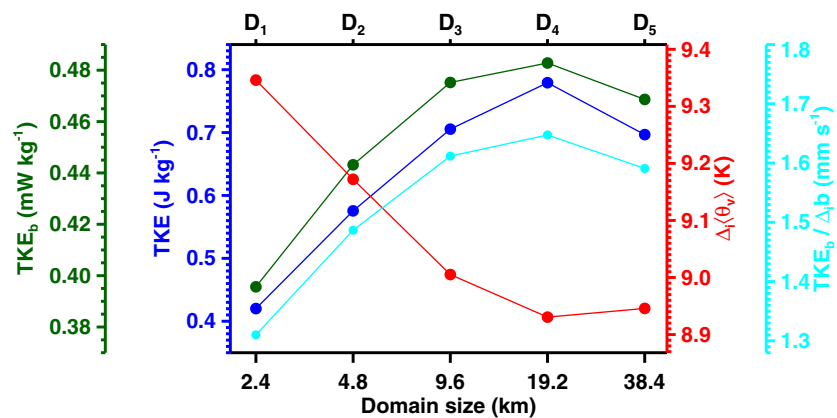
Figure 7. Boundary layer production of turbulence kinetic energy due to buoyancy TKE_b, boundary layer TKE, jump in virtual potential temperature across the inversion $\Delta_i \langle \theta_v \rangle$, and entrainment parameter $TKE_b / \Delta_i b$ (equation (2)), day 8–10.
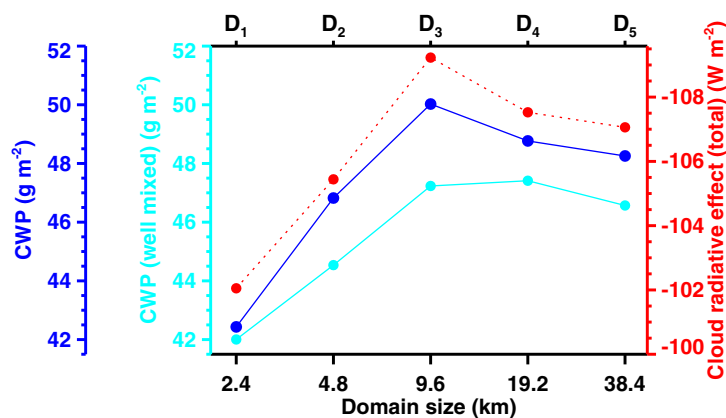
Figure 8. Cloud water path, cloud water path in a well-mixed boundary layer, and total cloud radiative effect, day 8–10.

entrainment rate and subsidence warming and drying are higher than on D_4 (Figure 6a), and boundary layer temperature and moisture adjust accordingly (Figure 6b).

3.2.2. Cloud Water Path and Cloud Radiative Effect

Based on first principles, cloud water path (CWP) increases as the boundary layer deepens, moistens, or cools, and vice versa. In addition to responding to these changes, CWP may also respond to changes in boundary layer circulation with domain size. The boundary layer shallows, cools, and moistens from D_1–D_4, and deepens, warms, and dries from D_4–D_5 (Figure 6). CWP increases from D_1–D_3 and decreases from D_3–D_5 (Figure 8). To explain the domain size dependence of CWP, we will quantify the effect of change in mean liquid water potential temperature θ_l, total moisture q_t, and in inversion height with domain size on CWP. A remaining domain size dependence of CWP will be attributed to change in circulation and the associated redistribution of temperature and moisture in the boundary layer. To determine the effect of mean θ_l and q_t and inversion height, we shall consider the CWP of the well-mixed (perfectly coupled) boundary layer, which is defined by these quantities only. Because θ_l and q_t are constant both under the well-mixed and the adiabatic assumption, the CWP of the well-mixed boundary layer can be calculated with an adiabatic parcel model. We calculated the CWP of the well-mixed boundary layer from boundary layer mean θ_l and q_t and the spatially resolved inversion height, as a function of time and location, by running the adiabatic parcel model between the surface and the inversion.

On D_1, the CWP and the CWP calculated in well-mixed conditions are nearly identical (Figure 8). From D_1–D_2 and from D_2–D_3, CWP increases by a greater increment than the CWP in well-mixed conditions. Hence as domain size increases from D_1 to D_3, circulation and the distribution of temperature and moisture become more effective in generating cloud water. From D_3–D_4, CWP in well-mixed conditions remains nearly constant (increases weakly). The effect of a cooler and moister boundary layer on CWP is therefore nearly compensated by the concurrent reduction of boundary layer depth (Figure 6). The actual CWP decreases from D_3 to D_4, hence circulation and the distribution of temperature and moisture change from D_3 to D_4 in a manner that makes them less effective in generating cloud water. From D_4–D_5, CWP decreases, more in well-mixed and less in actual conditions. The boundary layer therefore returns to a more effective circulation and temperature and moisture distribution with respect to generating cloud water.

The mechanisms underlying the domain size dependence of CWP can be described as follows: at a temporally constant aspect ratio of closed-cell mesoscale organization, the boundary layer becomes shallower, cooler, and moister as a result of reduced entrainment with increasing aspect ratio. As cell aspect ratio increases from ≈ 4 (D_1) to ≈ 16 (D_3), the increasingly cooler and moister conditions, together with an increasingly effective boundary layer circulation support a higher CWP. A further increase in aspect ratio to 32 (D_4) reduces the effectiveness of boundary layer circulation in generating cloud water, and CWP decreases against otherwise favorable boundary layer properties (temperature, moisture, and boundary layer depth). With domain size increasing from D_4 to D_5, the single mesoscale cell occupying the domain is replaced by a polydisperse cell population that evolves over the course of the diurnal cycle. Aspect ratio varies from ≈ 4 to 16 at dusk to 64 in the late afternoon, with an average value of 37. Entrainment and the inversion are higher and the boundary warmer and drier on D_5 relative to D_4. In response to these changes and to the accompanying change in circulation, CWP decreases from D_4 to D_5.

The domain size dependence of the cloud radiative effect (CRE) follows the domain size dependence of CWP (Figure 8). CRE increases from D_1–D_3, and falls to D_4 as boundary layer circulation becomes less effective in producing CWP. CRE falls further to D_5, following the adjustment of CWP to the emergence of

Table 1. Mean Values of Cloud Water Path and Total Cloud Radiative Effect (Day 8–10), Maximum-Minimum, and Sample Standard Deviation σ

	D_1	D_2	D_3	D_4	D_5	Max-Min	σ
CWP (g m^{-2})	42.9	47.3	50.5	49.3	48.8	7.6	3.0
CRE (W m^{-2})	-102.1	-105.4	-109.2	-107.5	-107.1	7.2	2.7

diurnally evolving mesoscale organization. CWP and CRE values are given in Table 1. Although the differences in mean boundary layer θ_l and q_t and in inversion height between domains are small, peaking at approximately 0.2 K, 0.15 g kg^{-1}, and 45 m, respectively (Figure 6), differences in CWP and CRE between domains are more substantial, peaking at 18% and 7%, respectively (from D_1 to D_3).

4. Discussion

4.1. Mesoscale Organization

With increasing cell aspect ratio, the boundary layer becomes more decoupled and cell scale circulation less effective in producing TKE and supplying moisture to the cloud layer (Figures 4 and 5c). Intermediate scale circulation, however, becomes more effective in producing TKE and supplying moisture to the cloud layer (Figure 5b). It strengthens from D_2 to D_4 (solid triangles in Figure 2) but is unable on these domains to establish itself continuously or to grow to larger sizes against circulation on the cell scale.

On D_5, the cell scale grows to an aspect ratio of 64 in the second half of the day (Figure 3b), at the cost of TKE production and moisture supply to the cloud layer: TKE production by buoyancy and cloud base moisture flux on the 38.4 km (aspect ratio 64) and 19.2 km scales (aspect ratio 32) on the domain D_5 languish in the closing hours of the day (Figures 2i and 2j). Concurrently, circulation emerges on D_5 on intermediate scales which until then has been suppressed by insolation. Hence mesoscale organization returns to a population of small cells in the evening because of the growth of the cell scale to an aspect ratio at which its TKE production and moisture supply to the cloud are weak, while circulation on smaller scales, emerging from the original cell structure, can establish itself. The next day (considering the scale evolution in Figures 2i and 2j as periodic, having approached a quasi-steady state, cf. supporting information Figures S9 and S10), mesoscale organization forms from cells with an aspect ratio of 16 (9.6 km scale). The growth of mesoscale organization from cells with an aspect ratio of 16 (as opposed to cells with larger aspect ratios) is consistent with the finding that in nearly equally favorable boundary layer conditions (temperature, moisture, boundary layer depth) for the maintenance of cloud water, they are less decoupled, and more effective in supplying moisture to the cloud and maintaining cloud water than cells with an aspect ratio of 32 (section 3.2.2).

The reduction with increasing cell aspect ratio of cell scale TKE production and moisture supply to the cloud on the cell scale and hence diminishing competitiveness of larger cells relative to smaller cells is a mechanism that can explain scale saturation in closed-cell mesoscale organization. Growing to larger cell sizes and aspect ratios, circulation on the cell scale fades to a point at which circulation on smaller scales, initially embedded into the original cell structure, becomes sufficiently strong to form new cells. In our simulations, the largest stable aspect ratio of closed-cell mesoscale organization is 32, while mesoscale organization with an aspect ratio of 64 cannot sustain itself against circulation emerging on smaller scales. The upper limit for the aspect ratio of closed-cell mesoscale organization is therefore to be found between 32 and 64. This is consistent with the observational limit of ≈ 40 [*Wood and Hartmann*, 2006].

4.2. Entrainment
4.2.1. Dynamical Driver

Entrainment is considered to scale with production of TKE due to buoyancy [*Lilly*, 1968; *Deardorff*, 1976]. Entrainment velocity parameterizations are therefore formulated as [*Stevens*, 2002]

$$w_e = \alpha \left(\frac{W}{\Delta_i b} \right) + \beta \tag{2}$$

where W is a measure of TKE production due to buoyancy and α and β are constants that depend on formulation. Inversion stability enters the parameterization with
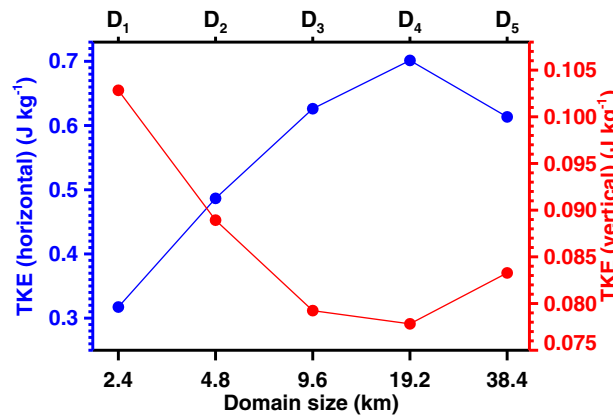
Figure 9. Boundary layer TKE horizontal and vertical components, day 8–10.

$$\Delta_i b = g \frac{\Delta_i \langle \theta_v \rangle}{\langle \theta_v \rangle (z_i)} \qquad (3)$$

where $\Delta_i \langle \theta_v \rangle$ is the virtual potential temperature jump across the inversion and $\langle \theta_v \rangle (z_i)$ the virtual potential temperature at the mean inversion height z_i. Brackets denote the instantaneous horizontal mean, g is Earth's surface gravity. We take W as the boundary layer buoyant production of TKE

$$\mathrm{TKE}_b = g \frac{\int_0^{z_i} dz \frac{\langle w' \theta_v' \rangle}{\langle \theta_v \rangle} \langle \rho \rangle}{\int_0^{z_i} dz \langle \rho \rangle} \qquad (4)$$

where ρ is air mass density. Entrainment velocity w_e is anticorrelated ($r = -1.00$) with TKE_b and $\mathrm{TKE}_b / \Delta_i b$ across domains (cf. Figures 6a and 7). Hence entrainment does not, in general, scale with buoyant production of TKE.

Figure 9 shows the partitioning of TKE into its horizontal and vertical parts. We denote the vertical component of TKE with TKE_w. w_e is correlated with TKE_w across domains ($r = 0.99$). w_e is also correlated with TKE_w over the course of the diurnal cycle on the individual domains (Table 2). This implies vertical motion as a driver of entrainment. *Kazil et al.* [2016] identified cloud layer updrafts and TKE_w associated with them as a key dynamical driver of entrainment in a growing boundary layer. In the quasi-steady state boundary layer investigated here, the correlation of w_e with TKE_w of updrafts is only imperceptibly higher than the correlation of w_e with TKE_w of downdrafts.

The slowing of entrainment with domain size on the domains D_1–D_4, which host a single dominant meso-scale cell, can be interpreted in terms of anisotropy of mesoscale turbulence. With increasing cell aspect ratio, anisotropy of turbulence grows, with more TKE residing in the horizontal and less in the vertical (Figure 9). Hence less TKE_w is available to drive entrainment.

A dependence of entrainment velocity on anisotropy of mesoscale turbulence or cell aspect ratio may be challenging to identify observationally. The entrainment rate varies by less than 10% with an eightfold change in cell aspect ratio (D_1–D_4) in our simulations (Figure 6a), less than variability and measurement errors [*Faloona et al.*, 2005; *Albrecht et al.*, 2016]. Variability in observed entrainment rates that may obscure a dependence on cell aspect ratio can arise from variability in surface heat and moisture fluxes [*Deardorff*, 1976], sedimentation and drizzle [*Ackerman et al.*, 2004; *Bretherton et al.*, 2007], and shear across the inversion [*Wang et al.*, 2008, 2012; *Katzwinkel et al.*, 2012; *Gerber et al.*, 2013].

4.2.2. Convective Velocity Scale

Turner [1968] and *Kato and Phillips* [1969] found in laboratory experiments of entrainment across an interface separating fluids of different density that entrainment velocity w_e scales as

$$w_e \propto w_*^3 / \Delta \rho \qquad (5)$$

$\Delta \rho$ is the density jump between the layers, and w_* is a velocity that characterizes turbulent motion and is determined ad hoc for a given system. *Deardorff* [1980] studied turbulence and entrainment in a stratocumulus-capped boundary layer using a three-dimensional model. He found the relationship

$$w_e \propto \frac{\mathrm{TKE}_b}{\Delta_i \langle \theta_v \rangle} \qquad (6)$$

which is the basis of entrainment parameterizations of the form (2). Based on the relationships (5, 6), *Deardorff* [1980] expanded the convective velocity scale for clear boundary layers [*Deardorff*, 1970a, 1970b]

Table 2. Correlation Coefficients Between Entrainment Velocity w_e and TKE_w (Vertical Component of TKE) and TKE_b (Buoyant Production of TKE) in the Boundary Layer Over the Course of a Diurnal Cycle (Day 10)[a]

	D_1	D_2	D_3	D_4	D_5
TKE_w	0.56	0.68	0.82	0.91	0.91
$\mathrm{TKE}_w / \Delta_i \langle \theta_v \rangle$	0.55	0.66	0.79	0.88	0.88
TKE_b	0.50	0.66	0.80	0.92	0.93
$\mathrm{TKE}_b / \Delta_i \langle \theta_v \rangle$	0.49	0.64	0.77	0.91	0.92

[a]$\Delta_i \langle \theta_v \rangle$ is the virtual potential temperature jump across the inversion.

$$w_* \propto \mathrm{TKE}_b^{1/3} \tag{7}$$

to the stratocumulus-capped boundary layer. The scalings are positive, meaning that higher turbulence is associated with a higher characteristic velocity and stronger entrainment.

To reflect the relationship between entrainment and the vertical component of TKE found in this work, the *Deardorff* [1980] entrainment scaling (equation (6)) can be re-written as

$$w_e \propto \frac{\mathrm{TKE}_w}{\Delta_i \langle \theta_v \rangle} \tag{8}$$

Deardorff [1980] hypothesized that it is intensity of vertical turbulence at the inversion that promotes entrainment and found a relationship at the inversion of his simulations analogous to equation (8). Combining equations (5) and (8) implies a stratocumulus-capped boundary layer convective velocity scale

$$w_* \propto \mathrm{TKE}_w^{1/3} \tag{9}$$

4.3. Domain Size Dependence

Previous studies have not identified a sensitivity of closed-cell stratocumulus cloud properties to simulation domain size. *de Roode et al*. [2004] determined that with increasing domain size between 3.2 and 25.6 km, mesoscale fluctuations increasingly contributed to vertical transport and to buoyant TKE production. Circulation with aspect ratios larger than 15 contributed more than one third of buoyant TKE production, similar to the results of this work (Figure 5c). Domain size had only a limited influence on the temporal evolution of mean quantities. *Duynkerke et al*. [2004] compared large eddy simulations of a stratocumulus cloud on a 2.5 km domain with a 25.6 km domain. Mesoscale organization formed on the larger domain, where cloud-top height was lower by approximately 20 m, but cloud water path evolved over the course of the simulations without a clear trend between the domains. Duynkerke et al. concluded that the mean state of the boundary layer was consistent in the two simulations. *Pedersen et al*. [2016] studied the stratocumulus-topped boundary layer with large eddy simulations on domain sizes between 3.5 and 21 km. They found no significant impact of domain size on cloud properties such as cloud fraction and cloud water path.

Possible explanations for the absence of a domain size dependence in previous studies are: (a) The dependence of entrainment and cloud water path on the grid spacing aspect ratio [*Kazil et al*., 2016; *Pedersen et al*., 2016]. *Duynkerke et al*. [2004] used different grid spacing aspect ratios on their small and large domain, which may have interfered with an effect of domain size. (b) A simulation duration that is too short for mesoscale organization to fully develop. The simulations of *de Roode et al*. [2004] extended over a duration of 8 h, and those of *Duynkerke et al*. [2004] over 10 h. *Pedersen et al*. [2016] conducted simulations over 6 h and noted that larger coherent structures could form in longer simulations. The simulations in this work give similar results in the first 6 h, after which domain D_1 diverges (supporting information Figure S2). Domain D_2 diverges after approximately 12 h. The larger domains D_3–D_5 have similar boundary layer and cloud properties for the duration of day 1.

The domain size dependence of cloud properties identified in the present work is smaller than variability between different LES models at fixed domain size. For the CGILS S12 CTL case considered in this study, the maximum inter-model difference is 32 g m^{-2} for CWP and 54 W m^{-2} for CRE [*Blossey et al*., 2013]. In our simulations, the maximum difference in the diurnal mean (day 8–10) between domain sizes is 7.6 g m^{-2} for CWP and 7.2 W m^{-2} for CRE, respectively (Table 1). Although a less prominent source of uncertainty than inter-model spread, several consequences of the domain size dependence have broader implications.

Stratocumulus clouds may exhibit a different susceptibility of cloud properties to aerosol, and precipitation may form more rapidly when simulated on large domains. The reason is in part the increase of CWP (Figure 3) and in part a broadening of the CWP probability distribution with domain size (supporting information Figure S4). A broadening of the CWP probability distribution in association with mesoscale organization in stratocumulus clouds was first identified by *Duynkerke et al*. [2004] and later by *Yamaguchi et al*. [2013]. Higher CWP values give rise to faster collision-coalescence and a more rapid drizzle and rain formation. *Yamaguchi et al*. [2015] found that formation of precipitation can initiate the stratocumulus-to-cumulus transition, however, sufficiently large domains must be used.

Table 3. Effect of Grid Refinement $G_1 \rightarrow G_2$ (At Constant Domain Size D_1) Versus Domain Size Increase $D_1 \rightarrow D_5$ (At Constant Grid Spacing G_1) on Entrainment Velocity w_e, Cloud Water Path CWP, and Cloud Radiative Effect CRE (Day 8–10)

	w_e (mm s^{-1})	CWP (g m^{-2})	CRE (W m^{-2})
D_1: $G_1 \rightarrow G_2$	$3.34 \rightarrow 3.06$ (−8%)	$42.9 \rightarrow 48.4$ (+13%)	$-102.1 \rightarrow -109.4$ (+7%)
G_1: $D_1 \rightarrow D_5$	$3.34 \rightarrow 3.15$ (−6%)	$42.9 \rightarrow 48.8$ (+14%)	$-102.1 \rightarrow -107.1$ (+5%)

The representation of clouds with cloud-resolving simulations embedded into large-scale models [*Parishani et al.*, 2017] may exhibit sensitivity to the resolution of the host model. A high host model resolution, corresponding to a small domain size of the embedded model, if smaller than the scale of mesoscale organization, may lead to an overestimation of entrainment and inversion height and to an underestimation of CWP, of the width of the probability distribution of CWP, and of the CRE in overcast stratocumulus clouds. An underestimation of CWP and of the width of its probability distribution may affect the susceptibility of cloud properties to aerosol, slow precipitation formation, and delay the transition from overcast stratocumulus clouds to broken stratocumulus and shallow cumulus clouds.

4.4. Resolution Versus Domain Size

Large eddy simulations of stratocumulus clouds converge with grid refinement toward reduced entrainment and higher cloud water path [*Stevens et al.*, 2005; *Pedersen et al.*, 2016]. In addition to the grid spacing G_1, we tested the grid spacing G_2 on the domain D_1. The grid refinement from G_1 to G_2 (at constant domain size) and an increase in domain size from D_1 to D_5 (at constant grid spacing) reduce w_e and strengthen CWP and CRE by a similar amount (Table 3) and produce a similar diurnal cycle in these quantities (supporting information Figure S11). The grid refinement maintains while the domain size increase broadens the width of the CWP probability distribution (supporting information Figure S12). Formation of precipitation may therefore respond differently to grid refinement and domain size increase.

In the considered case, the domain D_5 captures the relevant scales of mesoscale organization, while a much tighter grid spacing than G_2 would be required to capture the scales participating in entrainment: Eddies down to scales of ≈ 0.5 m are considered relevant for the entrainment process [*de Lozar and Mellado*, 2013, 2015]. A vertical grid spacing of ≈ 0.1 m would be required to resolve these eddies. Hence while mesoscale processes are computationally accessible at the grid spacings used in this work, a representation of scales involved in entrainment, even on the smallest considered domain, is a computational challenge. Scientific focus should guide compromise between grid refinement and domain size: Sufficiently large domains in studies of processes related to mesoscale organization and a fine grid spacing in studies of processes at the inversion appear a better fit for each respective context than combinations of domain sizes that are insufficient to capture mesoscale organization with grid spacings that produce unreliable entrainment.

5. Summary and Conclusions

We investigated closed-cell mesoscale organization and its relationship to entrainment and cloud properties in a boundary layer capped by a low, nonprecipitating stratocumulus cloud using large eddy simulations. The simulations were run over 10 periodic diurnal cycles during which mesoscale organization could fully develop and approach a quasi-steady state, on five domains ranging in size from 2.4 km × 2.4 km to 38.4 km × 38.4 km. The four smaller domains hosted a single cell with an aspect ratio that increased with domain size from approximately 4 to 32. On the largest domain, mesoscale organization evolved from small cells in the evening to large cells over the course of the next day, which faded in the afternoon and were replaced by small cells that reinitiated the cycle. The aspect ratio of circulation varied over the course of the day from ≈ 4–16 at dusk to 64 in the late afternoon. The diurnal cycle of mesoscale organization was driven by insolation, which suppressed circulation on scales below the cell scale but above microscale turbulence.

Analysis of the simulations on domains with an individual mesoscale cell revealed that with increasing cell size and aspect ratio, entrainment decreases and subsidence warming and drying weaken, and the boundary layer becomes shallower, cooler, and moister. Up to an aspect ratio of 16, the increasingly cooler and moister conditions together with an effective boundary layer circulation increase cloud water path (CWP). A further increase in aspect ratio to 32 reduces effectiveness of boundary layer circulation in generating cloud water, and CWP falls despite otherwise favorable boundary layer properties (temperature, moisture, and depth).

The boundary layer becomes more decoupled with increasing cell aspect ratio, and circulation on the cell scale becomes increasingly ineffective in supplying moisture to the cloud layer and producing turbulent kinetic energy (TKE) due to buoyancy. The reduction of TKE production and moisture supply to the cloud on the cell scale with increasing aspect ratio and hence a diminishing competitiveness of larger cells relative to smaller cells is a mechanism that can explain scale saturation in closed-cell mesoscale organization. Growing beyond a certain aspect ratio, circulation on the cell scale fades to the point at which circulation on smaller scales, initially embedded into the original cell structure, is sufficiently strong to form new cells. In our simulations, the largest stable aspect ratio of closed-cell mesoscale organization is 32, while meso-scale organization with an aspect ratio of 64 cannot sustain itself against circulation emerging on smaller scales. The upper limit for the aspect ratio of closed-cell mesoscale organization is therefore to be found between 32 and 64. This is consistent with the observational limit of ≈ 40.

Entrainment does not, in general, scale with buoyant production of TKE. Instead, the simulations show that entrainment correlates with the vertical component of TKE. This implies that vertical motion drives entrainment. As a corollary, the reduction of entrainment with increasing cell aspect ratio can be understood as a consequence of increasing anisotropy of mesoscale turbulence. With increasing cell aspect ratio, more TKE resides in the horizontal and less in the vertical, and hence less TKE is available in vertical motion to drive entrainment. Furthermore, this implies a convective velocity scale that is based on the vertical component of TKE rather than on buoyant production of TKE.

The (local) CRE differs by up to 7 W m^{-2} between the simulations on the different domains sizes. The domain size dependence of boundary layer and cloud properties is therefore a smaller source of uncertainty than large eddy simulation inter-model spread. However, several consequences with broader implications exist. The higher CWP and a broader CWP probability distribution on larger domains may give rise to faster formation of drizzle and precipitation. Stratocumulus clouds simulated on small domains may therefore have a different susceptibility of cloud properties to aerosol than on large domains. Faster drizzle and precipitation formation on larger domains may also enable or accelerate the transition from overcast stratocumulus to broken stratocumulus and shallow cumulus clouds which on smaller domains may be absent or proceed more slowly. The representation of boundary layer clouds in large-scale models with embedded cloud-resolving simulations may experience similar effects due to the embedded domain size.

In this work, we characterized mesoscale organization and its behavior in a shallow stratocumulus cloud in quasi-steady state. The climatically relevant subtropical marine stratocumulus cloud decks evolve, however, as they are advected equatorward across a gradient in sea surface temperature and subsidence strength. Surface fluxes increase, the boundary layer deepens and becomes more decoupled, and larger closed-cellular structures can form than in the shallow stratocumulus case studied here. Our results may not capture, quantitatively and qualitatively, mesoscale organization in these evolving stratocumulus decks. Their study may provide further insight.

References

Ackerman, A. S., M. P. Kirkpatrick, D. E. Stevens, and O. W. Toon (2004), The impact of humidity above stratiform clouds on indirect aerosol climate forcing, *Nature*, *432*, 1014–1017, doi:10.1038/nature03174.

Agee, E. M. (1984), Observations from space and thermal convection: A historical perspective, *Bull. Am. Meteorol. Soc.*, *65*, 938–949, doi:10.1175/1520-0477(1984)065<0938:OFSATC>2.0.CO;2.

Agee, E. M. (1987), Mesoscale cellular convection over the oceans, *Dyn. Atmos. Ocean*, *10*, 317–341, doi:10.1016/0377-0265(87)90023-6.

Agee, E. M., T. S. Chen, and K. E. Dowell (1973), A review of mesoscale cellular convection, *Bull. Am. Meteorol. Soc.*, *54*(10), 1004–1012, doi:10.1175/1520-0477(1973)054<1004:AROMCC>2.0.CO;2.

Albrecht, B., M. Fang, and V. Ghate (2016), Exploring stratocumulus cloud-top entrainment processes and parameterizations by using doppler cloud radar observations, *J. Atmos. Sci.*, *73*(2), 729–742, doi:10.1175/JAS-D-15-0147.1.

Atkinson, B. W., and J. W. Zhang (1996), Mesoscale shallow convection in the atmosphere, *Rev. Geophys.*, *34*, 403–431, doi:10.1029/96RG02623.

Blossey, P. N., C. S. Bretherton, M. Zhang, A. Cheng, S. Endo, T. Heus, Y. Liu, A. P. Lock, S. R. de Roode, and K.-M. Xu (2013), Marine low cloud sensitivity to an idealized climate change: The CGILS LES intercomparison, *J. Adv. Model. Earth Syst.*, *5*, 234–258, doi:10.1002/jame.20025.

Bretherton, C. S., P. N. Blossey, and J. Uchida (2007), Cloud droplet sedimentation, entrainment efficiency, and subtropical stratocumulus albedo, *Geophys. Res. Lett.*, *34*, L03813, doi:10.1029/2006GL027648.

Deardorff, J. W. (1970a), Convective velocity and temperature scales for the unstable planetary boundary layer and for Rayleigh convection, *J. Atmos. Sci.*, *27*(8), 1211–1213, doi:10.1175/1520-0469(1970)027<1211:CVATSF>2.0.CO;2.

Deardorff, J. W. (1970b), Preliminary results from numerical integrations of the unstable planetary boundary layer, *J. Atmos. Sci.*, *27*(8), 1209–1211, doi:10.1175/1520-0469(1970)027<1209:PRFNIO>2.0.CO;2.

Deardorff, J. W. (1976), On the entrainment rate of a stratocumulus-topped mixed layer, *Q. J. R. Meteorol. Soc.*, *102*(433), 563–582, doi:10.1002/qj.49710243306.

Deardorff, J. W. (1980), Stratocumulus-capped mixed layers derived from a three-dimensional model, *Boundary Layer Meteorol.*, *18*(4), 495–527, doi:10.1007/BF00119502.

de Lozar, A., and J. P. Mellado (2013), Direct numerical simulations of a smoke cloud-top mixing layer as a model for stratocumuli, *J. Atmos. Sci.*, *70*(8), 2356–2375, doi:10.1175/JAS-D-12-0333.1.

de Lozar, A., and J. P. Mellado (2015), Mixing driven by radiative and evaporative cooling at the stratocumulus top, *J. Atmos. Sci.*, *72*(12), 4681–4700, doi:10.1175/JAS-D-15-0087.1.

de Roode, S. R., P. G. Duynkerke, and H. J. J. Jonker (2004), Large-eddy simulation: How large is large enough?, *J. Atmos. Sci.*, *61*(4), 403–421, doi:10.1175/1520-0469(2004)061<0403:LSHLIL>2.0.CO;2.

Duynkerke, P. G., et al. (2004), Observations and numerical simulations of the diurnal cycle of the EUROCS stratocumulus case, *Q. J. R. Meteorol. Soc.*, *130*(604), 3269–3296, doi:10.1256/qj.03.139.

Faloona, I., D. H. Lenschow, T. Campos, B. Stevens, M. C. Van Zanten, B. Blomquist, D. Thornton, and A. Bandy (2005), Observations of entrainment in eastern Pacific marine stratocumulus using three conserved scalars, *J. Atmos. Sci.*, *62*(9), 3268–3285, doi:10.1175/JAS3541.1.

Feingold, G., R. L. Walko, B. Stevens, and W. R. Cotton (1998), Simulations of marine stratocumulus using a new microphysical parameterization scheme, *Atmos. Res.*, *47–48*, 505–528, doi:10.1016/S0169-8095(98)00058-1.

Feingold, G., I. Koren, H. Wang, H. Xue, and A. W. Brewer (2010), Precipitation-generated oscillations in open cellular cloud fields, *Nature*, *466*(7308), 849–852, doi:10.1038/nature09314.

Gerber, H., G. Frick, S. P. Malinowski, H. Jonsson, D. Khelif, and S. K. Krueger (2013), Entrainment rates and microphysics in POST stratocumulus, *J. Geophys. Res. Atmos.*, *118*, 12,094–12,109, doi:10.1002/jgrd.50878.

Graham, A. (1933), Shear patterns in an unstable layer of air, *Philos. Trans. R. Soc. London A*, *232*, 285–296, doi:10.1098/rsta.1934.0008.

Hartmann, D. L., and D. A. Short (1980), On the use of Earth radiation budget statistics for studies of clouds and climate, *J. Atmos. Sci.*, *37*, 1233–1250, doi:10.1175/1520-0469(1980)037<1233:OTUOER>2.0.CO;2.

Hartmann, D. L., M. E. Ockert-Bell, and M. L. Michelsen (1992), The effect of cloud type on Earth's energy balance: Global analysis, *J. Clim.*, *5*, 1281–1304, doi:10.1175/1520-0442(1992)005<1281:TEOCTO>2.0.CO;2.

Jones, C. R., C. S. Bretherton, and D. Leon (2011), Coupled vs. decoupled boundary layers in VOCALS-REx, *Atmos. Chem. Phys.*, *11*, 7143–7153, doi:10.5194/acp-11-7143-2011.

Kato, H., and O. M. Phillips (1969), On the penetration of a turbulent layer into stratified fluid, *J. Fluid Mech.*, *37*(4), 643–655, doi:10.1017/S0022112069000784.

Katzwinkel, J., H. Siebert, and R. A. Shaw (2012), Observation of a self-limiting, shear-induced turbulent inversion layer above marine stratocumulus, *Boundary Layer Meteorol.*, *145*, 131–143, doi:10.1007/s10546-011-9683-4.

Kazil, J., H. Wang, G. Feingold, A. D. Clarke, J. R. Snider, and A. R. Bandy (2011), Modeling chemical and aerosol processes in the transition from closed to open cells during VOCALS-REx, *Atmos. Chem. Phys.*, *11*(15), 7491–7514, doi:10.5194/acp-11-7491-2011.

Kazil, J., G. Feingold, H. Wang, and T. Yamaguchi (2014), On the interaction between marine boundary layer cellular cloudiness and surface heat fluxes, *Atmos. Chem. Phys.*, *14*, 61–79, doi:10.5194/acp-14-61-2014.

Kazil, J., G. Feingold, and T. Yamaguchi (2016), Wind speed response of marine non-precipitating stratocumulus clouds over a diurnal cycle in cloud-system resolving simulations, *Atmos. Chem. Phys.*, *16*, 5811–5839, doi:10.5194/acp-16-5811-2016.

Khairoutdinov, M. F., and D. A. Randall (2003), Cloud resolving modeling of the ARM summer 1997 IOP: Model formulation, results, uncertainties, and sensitivities, *J. Atmos. Sci.*, *60*(4), 607–625, doi:10.1175/1520-0469(2003)060<0607:CRMOTA>2.0.CO;2.

Krueger, A. F., and S. Fritz (1961), Cellular cloud patterns revealed by Tiros I, *Tellus*, *13*(1), 1–7, doi:10.1111/j.2153-3490.1961.tb00061.x.

Lilly, D. K. (1968), Models of cloud-topped mixed layers under a strong inversion, *Q. J. R. Meteorol. Soc.*, *94*(401), 292–309, doi:10.1002/qj.49709440106.

Mlawer, E. J., S. J. Taubman, P. D. Brown, M. J. Iacono, and S. A. Clough (1997), Radiative transfer for inhomogeneous atmospheres: RRTM, a validated correlated-k model for the longwave, *J. Geophys. Res.*, *102*, 16,663–16,682, doi:10.1029/97JD00237.

Moyer, K. A., and G. S. Young (1994), Observations of mesoscale cellular convection from the marine stratocumulus phase of "FIRE", *Boundary Layer Meteorol.*, *71*(1), 109–133, doi:10.1007/BF00709222.

Muhlbauer, A., I. L. McCoy, and R. Wood (2014), Climatology of stratocumulus cloud morphologies: Microphysical properties and radiative effects, *Atmos. Chem. Phys.*, *14*(13), 6695–6716, doi:10.5194/acp-14-6695-2014.

Orlanski, I. (1975), A rational subdivision of scales for atmospheric processes, *Bull. Am. Meteorol. Soc.*, *56*(5), 527–530.

Parishani, H., M. S. Pritchard, C. S. Bretherton, M. C. Wyant, and M. Khairoutdinov (2017), Toward low-cloud-permitting cloud superparameterization with explicit boundary layer turbulence, *J. Adv. Model. Earth Syst.*, *9*, 1542–1571, doi:10.1002/2017MS000968.

Pedersen, J. G., S. P. Malinowski, and W. W. Grabowski (2016), Resolution and domain-size sensitivity in implicit large-eddy simulation of the stratocumulus-topped boundary layer, *J. Adv. Model. Earth Syst.*, *8*(2), 885–903, doi:10.1002/2015MS000572.

Pino, D., H. J. J. Jonker, J. V.-G. d. Arellano, and A. Dosio (2006), Role of shear and the inversion strength during sunset turbulence over land: Characteristic length scales, *Boundary Layer Meteorol.*, *121*(3), 537–556, doi:10.1007/s10546-006-9080-6.

Shao, Q., and D. A. Randall (1996), Closed mesoscale cellular convection driven by cloud-top radiative cooling, *J. Atmos. Sci.*, *53*, 2144–2165, doi:10.1175/1520-0469(1996)053<2144:CMCCDB>2.0.CO;2.

Stevens, B. (2002), Entrainment in stratocumulus-topped mixed layers, *Q. J. R. Meteorol. Soc.*, *128*, 2663–2690, doi:10.1256/qj.01.202.

Stevens, B., et al. (2005), Evaluation of large-eddy simulations via observations of nocturnal marine stratocumulus, *Mon. Weather Rev.*, *133*(6), 1443–1462, doi:10.1175/MWR2930.1.

Stevens, D. E., A. S. Ackerman, and C. S. Bretherton (2002), Effects of domain size and numerical resolution on the simulation of shallow cumulus convection, *J. Atmos. Sci.*, *59*(23), 3285–3301, doi:10.1175/1520-0469(2002)059<3285:EODSAN>2.0.CO;2.

Turner, J. S. (1968), The influence of molecular diffusivity on turbulent entrainment across a density interface, *J. Fluid Mech.*, *33*(4), 639–656, doi:10.1017/S002211206800159X.

Wang, H., and G. Feingold (2009a), Modeling mesoscale cellular structures and drizzle in marine stratocumulus. Part I: Impact of drizzle on the formation and evolution of open cells, *J. Atmos. Sci.*, *66*(11), 3237–3256, doi:10.1175/2009JAS3022.1.

Wang, H., and G. Feingold (2009b), Modeling mesoscale cellular structures and drizzle in marine stratocumulus. Part II: The microphysics and dynamics of the boundary region between open and closed cells, *J. Atmos. Sci.*, *66*(11), 3257–3275, doi:10.1175/2009JAS3120.1.

Wang, S., J.-C. Golaz, and Q. Wang (2008), Effect of intense wind shear across the inversion on stratocumulus clouds, *Geophys. Res. Lett.*, *35*, L15814, doi:10.1029/2008GL033865.

Wang, S., X. Zheng, and Q. Jiang (2012), Strongly sheared stratocumulus convection: An observationally based large-eddy simulation study, *Atmos. Chem. Phys.*, *12*, 5223–5235, doi:10.5194/acp-12-5223-2012.

Wood, R., and D. L. Hartmann (2006), Spatial variability of liquid water path in marine low cloud: The importance of mesoscale cellular convection, *J. Clim.*, *19*(9), 1748–1764, doi:10.1175/JCLI3702.1.

Wyant, M. C., C. S. Bretherton, H. A. Rand, and D. E. Stevens (1997), Numerical simulations and a conceptual model of the stratocumulus to trade cumulus transition, *J. Atmos. Sci.*, *54*, 168–192, doi:10.1175/1520-0469(1997)054 < 0168:NSAACM>2.0.CO;2.

Yamaguchi, T., D. A. Randall, and M. F. Khairoutdinov (2011), Cloud modeling tests of the ULTIMATE-MACHO scalar advection scheme, *Mon. Weather Rev.*, *139*(10), 3248–3264, doi:10.1175/MWR-D-10-05044.1.

Yamaguchi, T., W. A. Brewer, and G. Feingold (2013), Evaluation of modeled stratocumulus-capped boundary layer turbulence with ship-borne data, *J. Atmos. Sci.*, *70*(12), 3895–3919, doi:10.1175/JAS-D-13-050.1.

Yamaguchi, T., G. Feingold, J. Kazil, and A. McComiskey (2015), Stratocumulus to cumulus transition in the presence of elevated smoke layers, *Geophys. Res. Lett.*, *42*, 10,478–10,485, doi:10.1002/2015GL066544.